Friction and Fretting Study of Thin Sheet Metal

Michael R. Hirsch, Dr. Richard W. Neu,

Woodruff School of Mechanical Engineering, Georgia Institute of Technology, Atlanta, GA, USA

Frank Popielas, Rohit Ramkumar,

Sealing Products Group, Dana Holding Corporation, Lisle, IL, USA

Abstract: Modern sealing technology in powertrain and exhaust applications of the automotive and heavy-duty industries utilizes Multi-Layer-Steel (MLS) gaskets for cylinder head gaskets (CHG) and exhaust gaskets. In light of more stringent requirements towards emissions and fuel economy, the increased application of shear forces on those gaskets due to vibration and thermal expansion have a major influence on the durability and wear of the gasket layers.

Computer Aided Engineering (CAE) plays a major role in development, design, and performance optimization for those applications. Traditionally used contact modeling through tie contact or a uniformly assigned constant friction coefficient using gasket elements can not reflect the real world well enough to meet modern requirements. Relevant friction data for thin stainless steel sheet material and its behavior as a function of time, load, and temperature is not available in the literature.

The mechanism of friction and fretting as applied to MLS gaskets and their applications in powertrain and exhaust systems was studied. Tribological testing techniques were developed for thin sheet metal and used to establish maps of the friction and wear behavior. This data creates the basis of the material properties and friction information for CAE input. Simulation techniques were developed duplicating first the laboratory tribological experiments to establish performance metrics before applying to the actual application environment.

Keywords: CAE, Sealing, CHG, MLS, exhaust gaskets, powertrain, contact, gasket element, fretting, tribology, durability, wear

1. Introduction

1.1 Role of friction in sealing applications for powertrain and exhaust applications

Modern sealing technologies in powertrain and exhaust applications of the automotive and heavy-duty industries are driven by increasingly more stringent requirements for emissions, fuel economy and noise behavior. Examples of sealing products for those applications are:

- Cylinder Head Gaskets (CHG)
- Exhaust Manifold Gaskets (EMG)
- Intake Manifold Gaskets (IMG)
- Turbo gaskets
- Exhaust Gas Recirculation (EGR) gaskets
- Down pipe gaskets, and many more.

Most of these gaskets are made out of multi-layer steel (MLS) components. They differentiate in their complexity and material (base metal and possible coatings) based on their application. Figure 1 shows the general different sealing elements for a MLS CHG application.

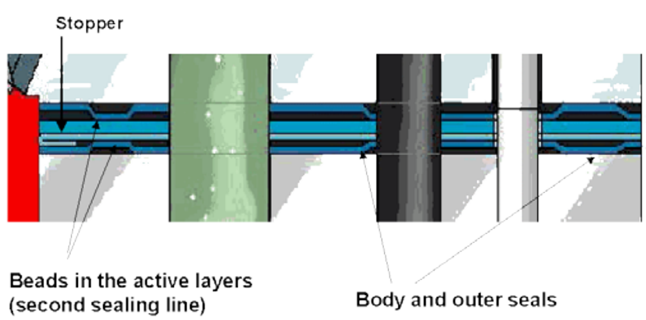

Figure 1. Cross section through a MLS CHG.

Due to their specific application, these components do not just have a simple sealing function but also play a major role as a system component, especially with their influence on the thermal management of the powertrain and exhaust system (Deshpande et al., 2009). Additional components having influence on the thermal balance of the overall system are shielding, covers and pans, as well as molded seals.

Traditionally, these components were designed and validated relatively independently from one another. But, with the main drivers being emission control and reduction, improvement in fuel economy, and noise control and reduction, new attention is paid to:

- Materials used for the hardware components
- New components for the exhaust and aftertreatment system
- Electronic component and system controls

As a result of this attention, powertrain systems have become lighter, more powerful, and smaller in displacement. Performance increases can be characterized by higher peak and average combustion pressures, improved torque characteristics, implementation of direct injection, and many more factors.

On the exhaust and aftertreatment side, over time hardware components like catalysts (CAT), turbo chargers, exhaust gas recirculation (EGR), active diesel particulate filters (aDPF), and Selective Catalytic Reduction (SCR) technology have emerged through rapid development to meet the legislative requirements (reduced emission regarding NO_x, CO and diesel particulates) placed on some markets and regions. In addition to the legislative requirement, the exhaust system must also meet the market expectations for cost, NVH and fuel efficiency (Deshpande et al., 2009).

As new technology was added to the exhaust system, the control, management, functionality, and robustness were continually refined and improved. Today's exhaust and after treatment systems have their own computer control unit and are often designed in the form of a cascade system, such as sequential turbo charging, flexible EGR, and active catalytic converters. The ultimate goal is to have a real-time, closed loop control system based on combustion measurements and exhaust system readings. This fully integrated system approach would also utilize a certain level of intelligence for continuous control and management (Deshpande et al., 2009).

Recent changes have resulted in a higher temperature environment. Besides a harsher thermal environment there are also additional consideration for higher back pressures and vibration issues. In general we expect to see maximum exhaust temperatures of 1050^{o}C for gasoline applications and 850^{o}C for diesel applications.

Based on the driving conditions, the engine packaging environment, and the shielding of specific areas, the skin and flange temperature of the components are continuously changing. With good air flow management around the engine compartment and exhaust system, the flange temperatures are normally lower than the exhaust gas temperature. However, once air flow becomes stagnated (heat soak), like idle conditions, in an encapsulated environment or aftertreatment operation, temperatures may actually rise beyond the maximum gas temperature. A good maximum temperature assumption is 1100ºC (Deshpande et al., 2009).

In order to achieve good start-up conditions one major goal is to get to the optimal thermal operating condition as fast as possible. Thus, a huge thermal gradient in the system is quite common. In addition, we see vibration of the additional attached components of 25 g or more, like turbochargers.

The factors discussed above result in a high friction environment. The main factors associated with friction are:

- Normal force
- Tangential displacement
- Temperature
- Surface conditions.

Normal force: Sealing joints always have fasteners as the main component providing the normal force. This force usually changes over time. The amount of force loss depends on the application.

Exhaust applications usually see higher load losses compared to a CHG application because of the higher temperatures involved. In addition, the force is rebalanced based on the gasket design. It is mainly focused where there are sealing features in the gasket. See Figure 1 as example for MLS CHG. The gasket design can drastically influence the normal load, which in turn influences the frictional behavior of the joint.

Tangential displacement: This factor is heavily influenced by thermal gradients and/or mismatches in the coefficients of thermal expansion of the materials in contact. Motion is constrained by dowels and fasteners for attached components.

Temperature: This factor is clearly a function of combustion, thermal management of the powertrain system, and the aftertreatment system. The temperature drives the tangential displacement and influences the type of wear that occurs (abrasive or adhesive).

Surface conditions: The main influencing factors are:

- Material of hardware components,
- Surface finish of those components,
- Lubrication or surface treatment of the mating components, like coatings, nitriding, etc.

As mentioned above, gaskets are directly exposed to these factors. Most of them can not be avoided. If not controlled, friction can become very high and cause fretting damage. Based on the application, it might result in pitting of the mating hardware component surface as shown in Figure 2, cracking of the gasket sealing between the mating hardware components as shown in **Error! Reference source not found.**(a), or wear of the gasket material as shown in Figure 3(b).

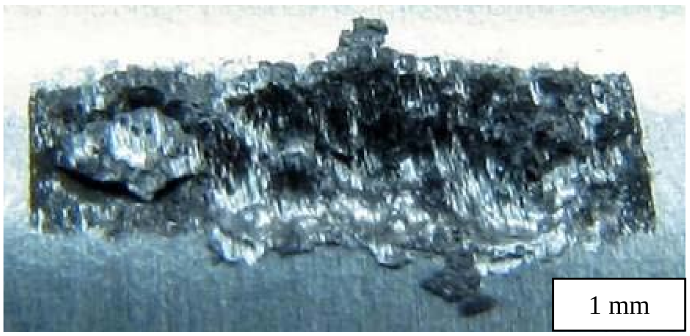

Figure 2. Pitting of the hardware surface due to high friction with the gasket resulting in fretting.

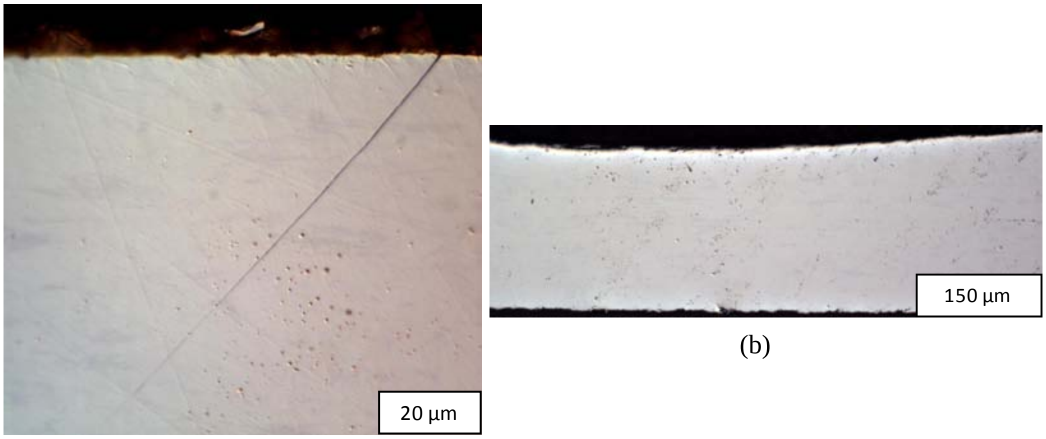

(a) (b)

Figure 3: (a) Cracking and (b) thinning of a gasket due to fretting.

Based on the above mentioned there is a huge need to be able to control friction without having negative impact on sealing function. There are many ways to solve this for gasket applications (Grafl et al., 1997). Many more ways have been and are being developed. The main issue though is that in order to develop the right solution for each application we need to understand much better the friction behavior for this type of application and how it can be predicted up-front in order to avoid high development costs and reduce development time.

1.2. Role of CAE in sealing applications and friction consideration

Since we are in a fast-moving environment where time-to-market, cost, “first-time-right”, design and quality are major driving factors in developing new designs, there is a need to look into new tools in development. Computer Aided Engineering (CAE) plays a major role. It has long proven its reliability for the different applications regarding accuracy. However, to achieve this level of accuracy requires a detailed understanding of the materials and their properties, which is especially challenging in the exhaust environment.

How CAE is implemented as an overall development tool plays a major role for its effectiveness regarding cost minimization and reduction in time-to-market. Influential factors are:

- Computer Hardware architecture
- Software performance and interaction with hardware
- Simulation process flow.

The approach for analyzing the different sealing joints and thereby the sealing system for a powertrain as a whole is accomplished by following step-by-step process outlined in Figure . Since there are several different components and different materials involved in the exhaust system, it is important to have a database with a collection of material properties at different thermal conditions. The approach can be slightly modified for the different parts of the exhaust system. The main driving factor here is the gas temperature, which dictates the different material types and the design direction that is chosen. Since several companies are involved in designing and manufacturing these different components, it is important to analyze the components together and to look at the interaction between them.

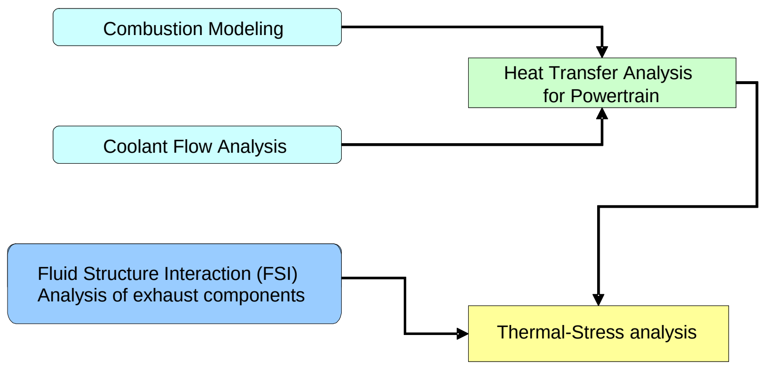

Figure 4. Analysis flow process.

Until recently, most of the structural analysis was done on a component or joint-by-joint basis due the cost of computation power and the software limitations. Now with multi-core computer technology and distributed memory processing technology available, larger and more detailed models can be created and analyzed within a much shorter time frame. The faster turnaround time also helps with incorporating design-of-experiments (DOE) which in turn fine-tunes design aspects not only for the gasket but also for components and material selection. With the opportunity to analyze the fluid-structure interaction problem occurring between the exhaust gases and the exhaust components, transient thermal profiles can be generated. Compared to steady state thermal profiles, transient thermal profiles show the largest thermal gradient during cold weather startup or water quenching (for vehicle underbody applications). The large thermal gradient provides the maximum motion between the component and the gasket, causing large wear of the gasket material. All this occurring at high temperatures can cause gasket thinning, possible leak paths, and eventual failure.

One of the primary joints where this analysis process was implemented was the joint between the head and the exhaust manifold. Usually the exhaust gasket was analyzed alone with the head and the manifold as the mating surface only, but how this joint impacted the cylinder head gasket functionality was rarely studied. Analyzing the cylinder head gasket while including the exhaust gasket and the intake gasket along with their respective manifolds shows how the different bolted joints behave together and how the thermal stress in the cylinder head affects the intake joint and exhaust joints or vice versa. Components bolted to the cylinder head also influence the deformation of the cylinder head, and therefore affect the thermal balance of the whole system.

Fretting and friction play a central role in the development of high temperature sealing solutions. The extreme changes in operating temperature can cause potentially damaging friction forces. These forces are introduced by thermal expansion and contraction and are magnified by the dissimilar nature of the joint and gasket materials. Most commercially available friction analysis procedures provide a low-temperature short-term result. It is necessary to understand how the friction coefficients behave over thousands of thermal cycles as surface conditions are altered due to mechanical wear. A thermal cycle is a relatively slow phenomenon.

In typical FE analysis, the friction coefficient between two contacting surfaces are kept constant. Previously, lower friction coefficient values were used to make the solution convergence easier. But with the advancement of the contact solutions by the FE solvers, more realistic values are being used. This analysis provides better accuracy, but does not take into consideration the change in surface condition or change in friction coefficient due to changes in contact pressure and temperature. To attain more accuracy in these analyses, more study is required as well as changes in friction model, likely using a user subroutine model based on the test results, which includes an anisotropic friction model or inclusion of stick-slip based friction model. The stick slip model should be derived from the fretting map generated from study described below.

In current day analyses, gasket elements are used to study the sealing behavior of the joint under variety of conditions. These elements provide limited capability when compared to continuum elements for bending behavior and wear modeling. Sub-modeling or detailed joint analysis need to be performed to obtain more accurate results, which can predict the amount of motion due to thermal gradient. The motion generated can be used to calculate the wear of the metal. User subroutines can also be used to incorporate the wear characteristics which take into account the contact pressure, change in friction coefficient over time and temperature.

1.3. Friction and fretting for thin sheet metal as we know it

Austenitic stainless steel is widely used in MLS gasket applications because of its desirable combination of strength, ductility, and corrosion resistance. There have been many studies on the fretting behavior of austenitic stainless steel because of its widespread use, the common occurrence of fretting, and the potential severity of the resulting damage. However, only one fretting study has been performed using AISI 301 stainless steel in the full hard condition (Hirsch and Neu, 2008).

The sheets used for MLS gaskets are typically less than 0.5 mm thick. Thickness effects in fretting have received very little attention in the literature for thicknesses less than 1 mm (Hutson et al., 2001). This is partly because the common fretting test methods are not well suited for testing thin sheets. However, recent work has developed a method for testing thicknesses representative of gasket materials (Hirsch and Neu, 2008).

The two main damage mechanisms associated with fretting are fatigue and wear. Both mechanisms are strongly related to the conditions at the interface of the contacting bodies. Wear is driven by the energy dissipated due to friction, and fatigue damage is driven by the cyclically varying multiaxial stress field resulting from contact. There have been many studies which have sought to model the damage due to fretting using computational models. The challenge is to accurately model the conditions at the interface since both damage mechanisms are very sensitive to the contact conditions. The magnitude of slip has a large effect on the wear rate and is sensitive to the stiffness of the system, the magnitude of the displacement, the contact force, and the COF, which also varies with the conditions. Also, the gradient in stress and strain resulting from fretting is severe, making it difficult to determine the level of fatigue damage.

2. Friction and fretting

Fretting occurs when two bodies in contact undergo low amplitude relative slip. Components damaged by fretting can exhibit a drastic reduction in fatigue performance due to the acceleration of fatigue crack nucleation, called fretting fatigue. Fretting also results in material removal which is called fretting wear. The type and extent of fretting damage is dependent on the material combination and is affected by many parameters, making it difficult to design against fretting. These parameters include the contact pressure, displacement amplitude, coefficient of friction (COF), temperature, geometry of contact, contacting materials and their properties, and surface treatments (Waterhouse, 1992).

There are three situations that can occur during a fretting cycle which are referred to as contact conditions: Partial Slip (PS), Gross Slip (GS), and Reciprocating Sliding (RS). PS is the condition where there is no relative motion between the contacting bodies in the center of contact (stick) while one or both edges of the contact experience a small amount of relative motion (slip). GS results when the entire contact area experiences slip. RS is an extreme case of GS where the displacement range is greater than the contact width so that no single location in the contact area remains in contact with the other body for an entire cycle. A plot of tangential force versus displacement at the contact (hysteresis loops) are considerably different for PS and GS contact conditions. PS results in an elliptical shaped hysteresis loop, while GS results in a parallelogramic hysteresis loop as shown in Figure .

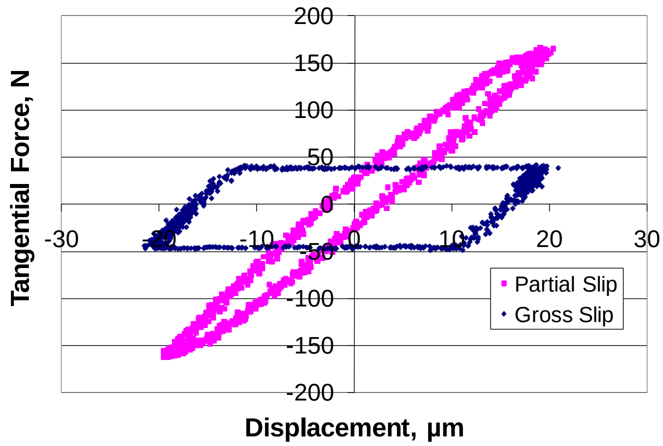

Figure 5. Representative hysteresis loops for partial slip (PS) and gross slip (GS) contacts.

The possible running conditions describing the contact condition over a period of time are shown in Figure (a). The Partial Slip Regime (PSR) is the situation where the contact condition is PS for the entire time period, Mixed Fretting Regime (MFR) or Mixed Slip Regime (MSR) is where the contact condition starts as GS and later transitions to a PS running condition, and Gross Slip Regime (GSR) is where the contact condition is GS for the entire time period. The contact condition that occurs for a certain contact pair depends on the contact force and displacement amplitude.

The type of damage that occurs due to fretting is different for the various running conditions. This relationship can be represented by a Material Response Fretting Map (MRFM) as shown in Figure (b) (Blanchard et al., 1991). The area inside the hysteresis loop is the energy dissipated. The energy dissipated is higher in the GSR, thus resulting in a higher wear rate. As the energy dissipation rate decreases as the running condition transitions to the MFR and then PSR, the wear rate decreases and cracking becomes the dominant damage mechanism.

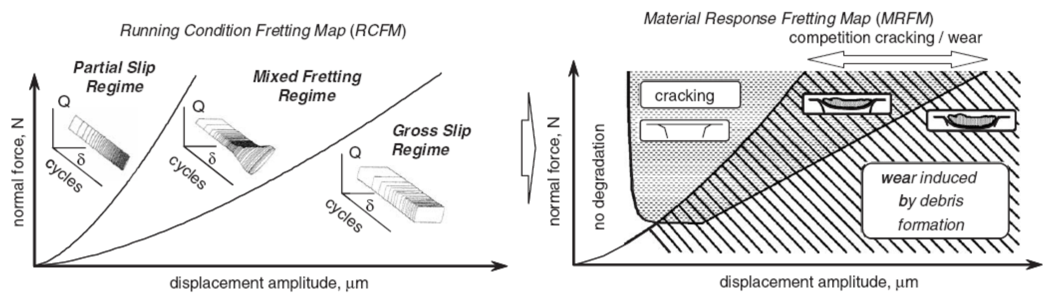

Figure 6. (a) Running condition fretting map with corresponding friction logs and (b) material response fretting map (Fouvry et al., 2006).

The compliance of the test system and specimens has a large effect on the measured response. The compliance controls the slope of force reversals in the hysteresis loops. An ideally rigid system would result in hysteresis loops with vertical force reversals, while increasing the compliance of the test system causes the slope to decrease. Therefore, the compliance affects the contact condition for a fixed contact force and displacement amplitude which must be taken into account in any simulation.

3. Experimental investigation

3.1 Procedure

Experiments were conducted to determine the friction response and material degradation behavior as a function of contact force and displacement amplitude in order to calibrate and verify the FE model. The experimental configuration used is shown schematically in Figure (a). AISI 301 stainless steel dog-bone specimens with a 205 µm thickness and 4.76 mm width were secured in the holders shown in Figure (b). The PTFE layer is 89 µm thick and was adhered to the holder to prevent fretting damage between the specimen and the holder. The moving specimens used were either AISI 52100 bearing steel or ANSI A356 cast aluminum cylinders with a 10 mm radius resulting in line contact. Line contact was used to allow for a simplified 2D plane strain FE model. Tests were conducted at 10 Hz at room temperature in laboratory air for 10^4 cycles. Contact force and displacement amplitude were controlled and tangential force was measured. Three contact forces and 12 displacement amplitudes were used to generate a range of running conditions that are representative of the conditions seen in service of MLS gaskets. Thus, the COF for this contact pair was determined as a function of the contact force and displacement amplitude.

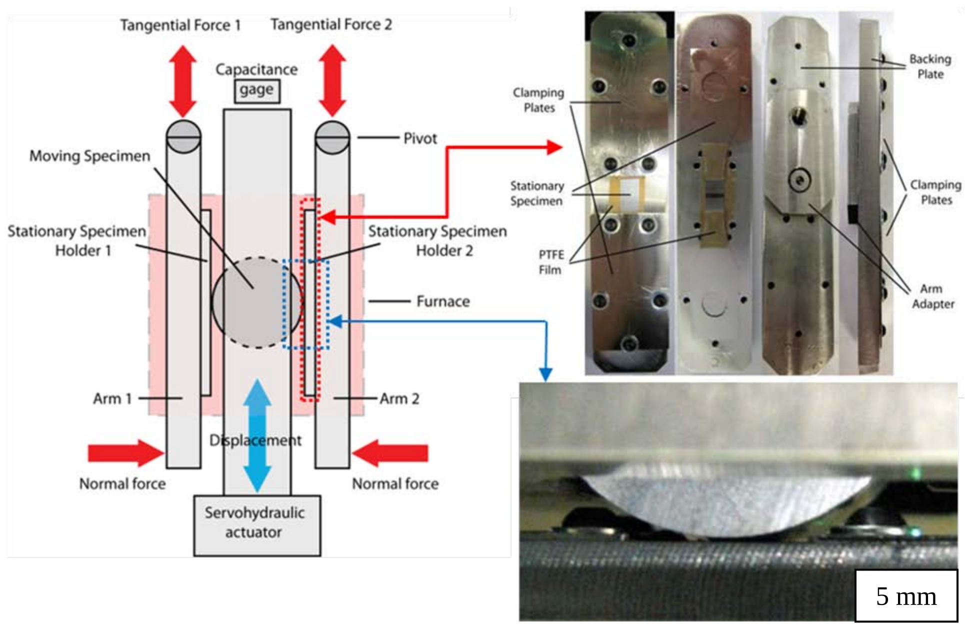

Figure 7. Experimental configuration: (a) fretting machine, (b) specimen holder, (c) local contact region.

Fatigue damage due to fretting was characterized by subjecting the stainless steel specimens to uniaxial fatigue loading following the fretting test. The details of the study are described elsewhere (Hirsch and Neu, 2008). Thus, the extent of fretting fatigue damage was determined as a function of contact force and displacement amplitude.

Wear damage due to fretting was characterized by sectioning the specimen and measuring the change in surface profile at the contact location with an optical microscope. Visual inspection of the specimen surface provided information about whether abrasion, adhesion, or delamination was the dominant wear mechanism. Thus, the fretting wear behavior was characterized as a function of contact force and displacement amplitude.

A FE model of the entire experimental configuration to examine the contact of interest would be overly complex. Therefore, the small region around the contact was chosen as the basis for the FE model which is shown in Figure (c). This simplification greatly reduces the computational expense of the analyses.

3.2 Experimental results

The running condition response in a fretting test between 301 stainless steel and 52100 steel with a displacement amplitude of 100 µm is shown in Figure 8. The COF begins at a low value and increases by a factor of four to reach a stabilized value after approximately 10^3 cycles. Tests were run for 10^4 cycles to ensure that a stabilized response was reached.

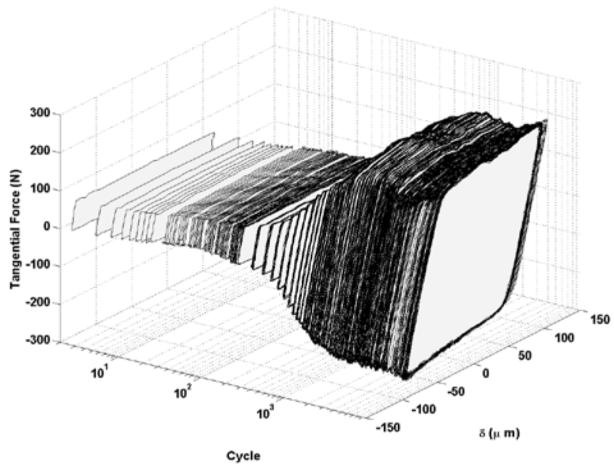

Figure 8. Friction log for contact between 301 stainless steel and 52100 steel with a contact force of 255 N and displacement amplitude of 100 µm.

The tangential force ratio, defined as the tangential force divided by the normal force, after 10^4 cycles for a normal force of 255 N and various displacement amplitudes is shown in Figure 9. The running condition is indicated for each case. For contact with A356 aluminum, the highest tangential force was found to occur in the MSR near the transition to the GSR. For contact with 52100 steel, the highest tangential force was found to occur in the GSR relatively far from the MSR-GSR transition displacement amplitude. Note that under sliding conditions, the tangential force is often called the friction force.

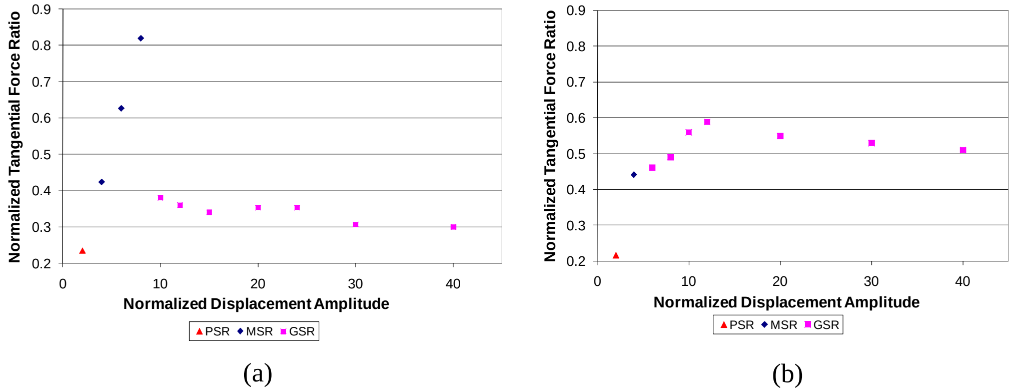

Figure 9. Normalized steady state tangential force ratio for contact with (a) A356 aluminum and (b) 52100 steel for a normal force of 255 N.

The subsequent fatigue life for a normal force of 255 N and various displacement amplitudes is shown in Figure 10. No reduction in fatigue life due to fretting was found for a normalized displacement amplitude of 2 for contact with 52100 steel or 8 for contact with A356 aluminum. Life was shorter for higher displacement amplitudes, indicating that more fretting damage occurred for those conditions. A significant amount of wear occurred at the higher displacement amplitudes when contacted with 52100 steel. The decreased thickness of the specimen is partially responsible for the reduction in life. When an A356 aluminum moving specimen was used, aluminum transferred to the stainless steel specimen via adhesive wear. The layer of deposited aluminum may have helped protect the sample from damage at higher displacement amplitudes, thus resulting in a longer subsequent fatigue life.

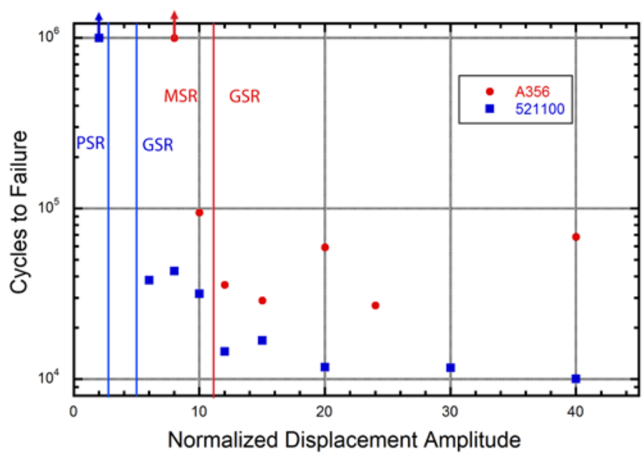

Figure 10. Subsequent fatigue life for various displacement amplitudes and a normal force of 255 N.

4. Modeling procedure

4.1 Verification model

A simple model was created using ABAQUS/CAE to represent the case of a cylinder sliding on a half-space for which a well established analytical solution exists in order to verify the contact formulation. The solution for the surface tractions for a cylinder sliding on a half-space is given by (Johnson, 1985):

For x < |a|,

$$S_{11} = -p_0\left(\sqrt{1-\frac{x^2}{a^2}} + \frac{2\mu x}{a}\right)$$
$$S_{22} = -p_0\sqrt{1-\frac{x^2}{a^2}}$$
$$S_{12} = -\mu \cdot p_0\sqrt{1-\frac{x^2}{a^2}}$$

for x < -a,

$$S_{11} = -2\mu p_0\left(\sqrt{\frac{x^2}{a^2}-1} + \frac{x}{a}\right)$$
$$S_{22} = 0$$
$$S_{12} = 0$$

for x > a,

$$S_{11} = 2\mu p_0\left(\sqrt{\frac{x^2}{a^2}-1} - \frac{x}{a}\right)$$
$$S_{22} = 0$$
$$S_{12} = 0$$

where

$$p_0 = \sqrt{\frac{PE^*}{\pi R}}$$
$$E^* = \left(\frac{1-\upsilon_1^2}{E_1} + \frac{1-\upsilon_2^2}{E_2}\right)^{-1}$$
$$a = \sqrt{\frac{4PR}{\pi E^*}}$$

where x is the distance along contact from the center and the direction in which the cylinder is sliding, a is the contact half width, μ is the coefficient of friction, P is the force per unit length of contact, E_1 and E_2 are the elastic moduli of each material, υ_1 and υ_2 are the Poisson's ratios of each material, R is the radius of the cylindrical body, the 1 direction is horizontal, and the 2 direction is downward.

A schematic of the verification model with boundary conditions is shown in Figure 11. The moving specimen was modeled as a half-cylinder due to symmetry. The vertical force P and horizontal displacement d are prescribed at a reference point on a rigid layer at the top of the moving specimen. The rigid layer distributes the point force along the top of the moving specimen and allows for the rotation to be fixed so that the friction at contact causes only translation.

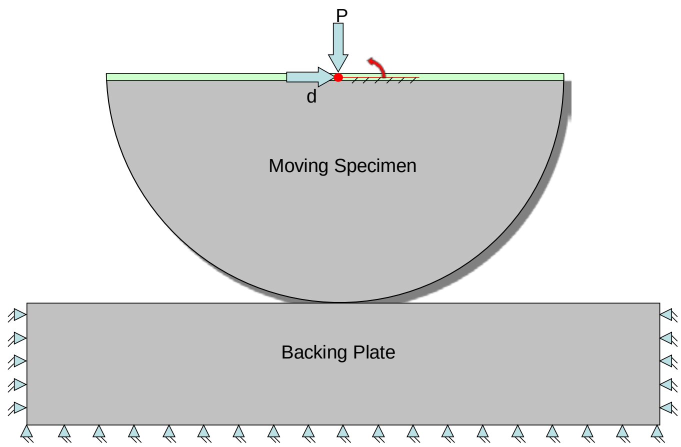

Figure 11. Schematic of verification model.

The verification simulation was performed using Abaqus/Standard and was broken into the three steps shown in Figure 12. The indentation of the cylinder was divided into two steps. First, a downward displacement of 1 μm was imposed at the reference point at the top center of the moving specimen to initiate contact. The second step removed the downward displacement constraint, and imposed a downward force at the reference point. During indentation, displacement of the rigid layer in the lateral direction was not allowed. This two-step method of applying the normal force greatly increased stability compared to a direct force-controlled indentation. The third step imposed a displacement at the reference point at the top center of the moving specimen in the horizontal direction to result in sliding between the bodies.

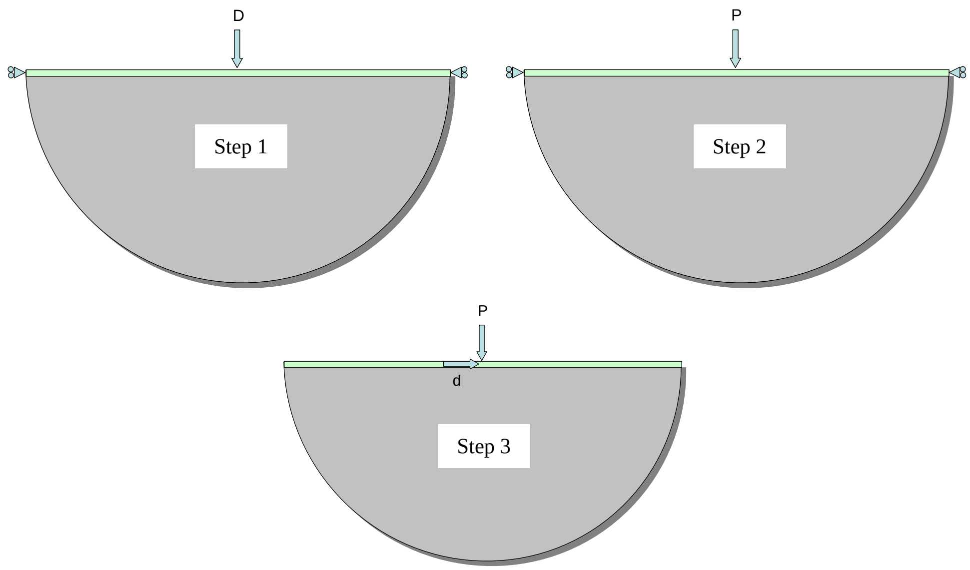

Figure 12. Steps used for the verification simulation.

There are several calculation methods for both the normal and tangential contact behavior with varying levels of complexity, computation time and stability. Surface-to-surface contact was used with a finite sliding formulation and hard contact pressure-overclosure behavior. Hard contact enforces no penetration of the bodies, that there is no force between the bodies if they are not in contact (no adhesion effects), and allows an infinite pressure to be transferred between the master and slave surfaces. The backing plate was chosen as the master surface and the moving specimen was chosen as the slave surface.

The Lagrange Multiplier friction formulation was used for the tangential contact behavior. The Lagrange Multiplier friction formulation enforces the sticking constraints at an interface between two surfaces so there is no relative motion unless $\tau = \tau_{critical}$. The Lagrange Multiplier formulation was used because of its ability to enforce exact stick unlike penalty friction that permits relative motion of the surfaces (an "elastic slip") when they should be sticking (i.e., $\tau < \tau_{critical}$). However, using Lagrange Multiplier contact formulation decreases stability and increases computation time. Isotropic friction was used for the verification analysis, with no dependence on pressure, velocity, or temperature. The constant COF was chosen to be 0.55 based on experimental data. The Penalty constraint enforcement method was used for the normal contact behavior to reduce the computation difficulty. It was determined that this did not compromise accuracy since the tangential contact behavior was the primary focus.

All components were modeled as elastic with isotropic material properties. The material properties used for each component are shown in Table 1. It was determined that an elastic analysis was sufficient for the conditions that were modeled. Plastic or anisotropic material behavior could be incorporated if desired.

Table 1. Material properties of modeled components.

Component	Material	Poison's ratio	Elastic Modulus
Moving Specimen	52100 Steel	0.30	210 GPa
Moving Specimen	A356 Aluminum	0.33	70 GPa
Stationary Specimen	301 Stainless Steel	0.30	195 GPa
PTFE Layer	PTFE	0.46	0.5 GPa
Backing Plate	304 Stainless Steel	0.30	195 GPa

The mesh of the verification model is shown in Figure 13. The mesh is denser in the region of contact where there is a large stress gradient during sliding. In that area, elements are 2D plane strain linear quadrilateral reduced integration (CPE4R) meshed using a structured technique. Linear elements were used because of convergence issues that arise with using quadratic elements in contact simulations. Reduced integration elements were used since strains and stresses are calculated at the locations that provide optimal accuracy (Barlow points) while simultaneously reducing computation time and storage requirements. In the contact area the mesh is progressive so that the elements are smaller near contact. Areas other than the region near contact were meshed using a quadrilateral dominated meshing scheme. By allowing triangular elements (CPE3) to be used in areas where the solution was less critical, fewer elements had poor aspect ratios because of the added freedom. These regions were not meshed using the structured meshing routine, but rather free meshing to aid in mesh transition between the densely meshed area and the coarsely meshed area. The size of the mesh in the dense-mesh region was decreased until there was acceptable correspondence between the analytical solution and the computational solution along a path on the contact surface of the pseudo-half-space. The results for a 5 μm, 2 μm, and 1 μm mesh size compared to the analytical solution are shown in Figure 14.

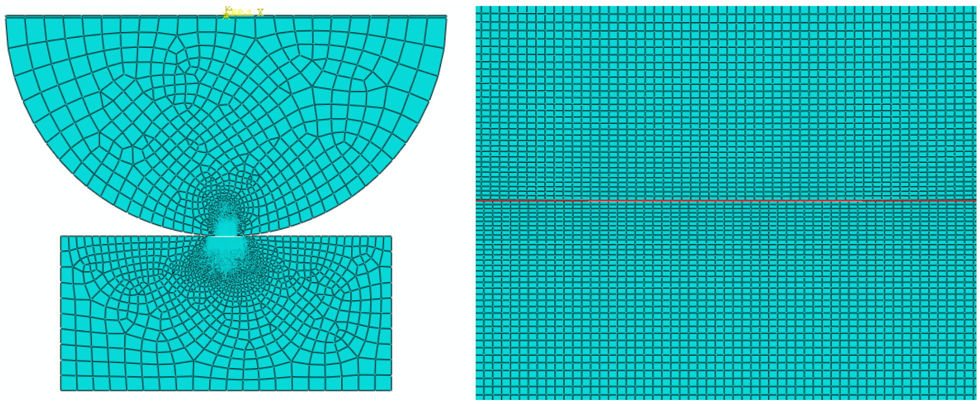

Figure 13. Mesh of the verification model with both zoomed-out and zoomed-in views where the red line shows the boundary between the top and bottom bodies.

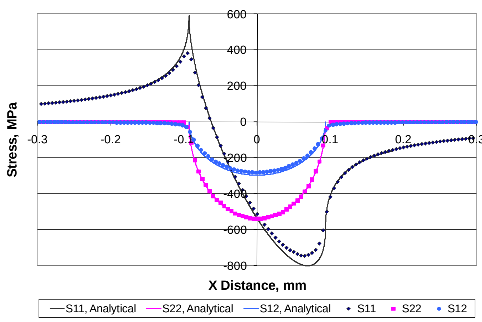

(a)

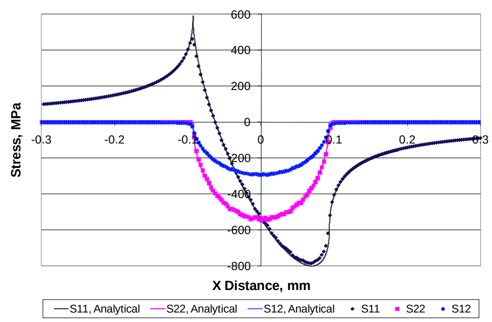

(b)

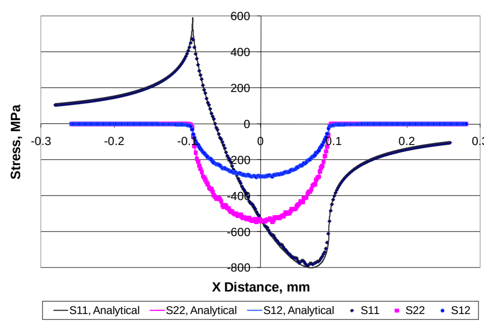

(c)

Figure 14. Comparison of analytical solution to computational solution of the stresses along the surface of the stationary specimen while the moving specimen translates to the right using three different mesh sizes in the dense mesh region: (a) 5 μm, (b) 2 μm, and (c) 1 μm.

The mesh needed to be very fine in order to capture the sharp gradient in the S_{11} stress component at the trailing edge of contact (right side in Figure 14). Based on the analytical solution, the value of S_{11} at that location is 590 MPa. The 5 µm mesh size case shows a peak stress of 380 MPa at that location. Using a 2 µm mesh size, a value of 461 MPa was calculated. The 1 µm mesh size case showed a value of 473 MPa. Because the 1 µm case still did not capture the extent of the stress concentration and was only marginally closer than the 2 µm case with a large computation cost penalty, the mesh size for the final model was chosen to be 2 µm. Using an element size of 2 µm resulted in 35,300 CPE4R elements in the contact region on the half-cylinder and 55,800 CPE4R elements in the contact region on the pseudo-half-space. A total of 106,350 elements were used: 105,718 CPE4R and 632 CPE3. Although the peak S_{11} stress captured by the FEA was significantly lower than the analytical model (22% lower), it is not critical to capture the peak stress since it occurs over such a small volume. It is the average value of stress over a volume that is important, since fatigue is a process that occurs over a volume of material.

4.2 Model of the experimental configuration

The model of the experimental configuration was based on the region immediately surrounding the contact as shown in Figure (c) since it would be impractical to model the entire test system. However, the stiffness of the test system has a large effect on the contact condition, and therefore the material response. Therefore, layers of compliant material were added to the sides of the model to account for the machine compliance.

The complete model is shown schematically in Figure 15. The model is an assembly of three parts: the moving specimen with the rigid layer, the stationary specimen with a compliant layer at each end, and the bottom body which includes a PTFE layer, backing plate, and a compliant layer at each side of the backing plate. The moving specimen has a radius of 10 mm, the stationary specimen has a thickness of 205 µm, and the PTFE layer has a thickness of 89 µm. The bodies were partitioned so that the separate material properties could be prescribed. There are two contact interactions. The contact interaction between the moving specimen and the stationary specimen was Lagrange Multiplier for the tangential contact behavior and Penalty constraint enforcement was used for the normal contact behavior. The stationary specimen was chosen as the master surface for this contact interaction because it experiences more deformation than the moving specimen. For the interaction between the stationary specimen and the PTFE layer, a Penalty constraint enforcement method was used for the normal behavior and a Penalty friction formulation was used for the tangential behavior since it was not critical to enforce exact stick at that location at the expense of stability. The PTFE layer was chosen as the master surface since it experiences more deformation than the moving specimen. The first three steps used were the same as for the verification model. Two additional steps were added where the displacement direction was reversed so that the moving specimen translated to the left and then reversed again to complete one full fretting cycle.

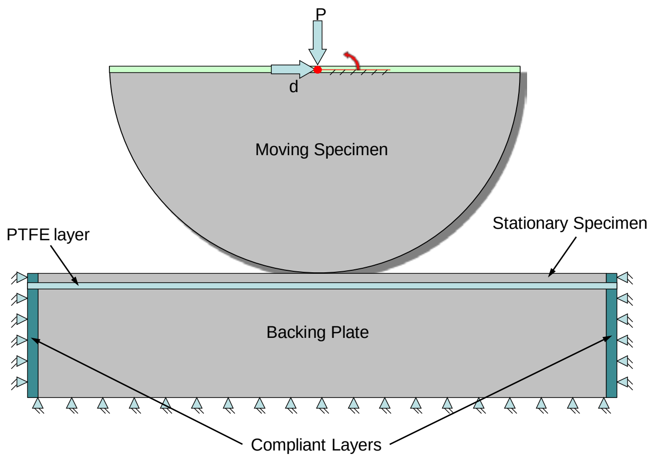

Figure 15. Schematic of the experimental configuration model.

The mesh of the final model was created similarly to that of the verification model and is shown in Figure 16. There were a total of 40,219 CPE4R elements and 466 CPE3 elements in the moving specimen, 41,955 CPE4R and 64 CPE3 in the stationary specimen (41,200 of which were in the contact region), 468 CPE4R in the PTFE layer, and 4,996 CPE4R and 92 CPE3 elements in the backing plate. Plane strain elements were used because of the in-plane symmetry and relatively large out-of-plane dimension of the configuration compared to the thickness of the specimen.

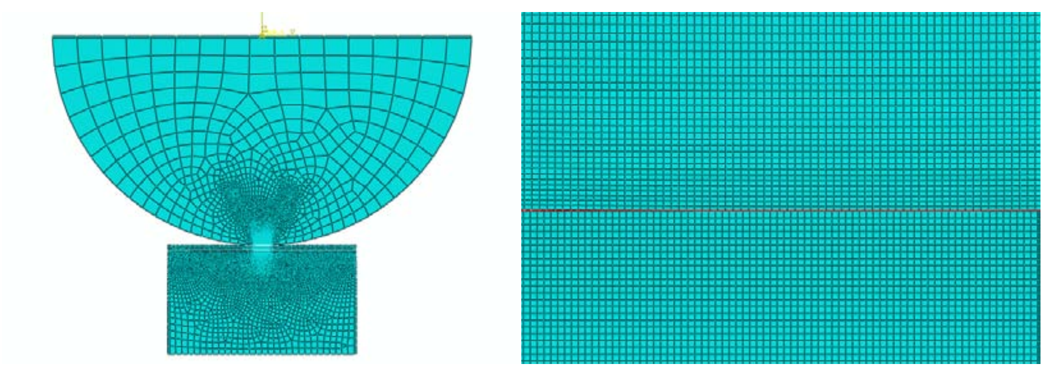

Figure 16. Mesh of the experimental configuration model.

The stiffness of the compliant layers that is representative of the test configuration was determined by comparing the slope of the hysteresis loops generated from the model to the slope of the hysteresis loops measured in experiments. Hysteresis loops were determined from the model by plotting the horizontal reaction force at the reference node where the displacement was applied versus the displacement at the same point. Adjustments were made to the stiffness of the compliant layers iteratively until correspondence was achieved.

The COF specified at the interaction between the PTFE layer and the stationary specimen was also determined iteratively by comparison of model and experimental hysteresis loops. The value used affects the hysteresis loop width, since it is representative of the amount of energy dissipated due to friction. The COF at that interface also affected the slope of the hysteresis loop since a higher COF results in higher stiffness. The COF at the contact between the moving and stationary specimens was specified as the value measured experimentally for the certain combination of normal force and displacement amplitude.

An example of a hysteresis loop generated from a model with an incorrect PTFE-stationary specimen COF and compliant layer stiffness is shown in Figure 17. In this example, it is evident that the COF is too high since the wider loop shows more energy dissipation. Also, the average slope of the model hysteresis loop (the slope of a straight line connecting the minimum value to the maximum value) is lower than the average slope of the measured hysteresis loop. This indicates that the stiffness of the compliant layers is too low.

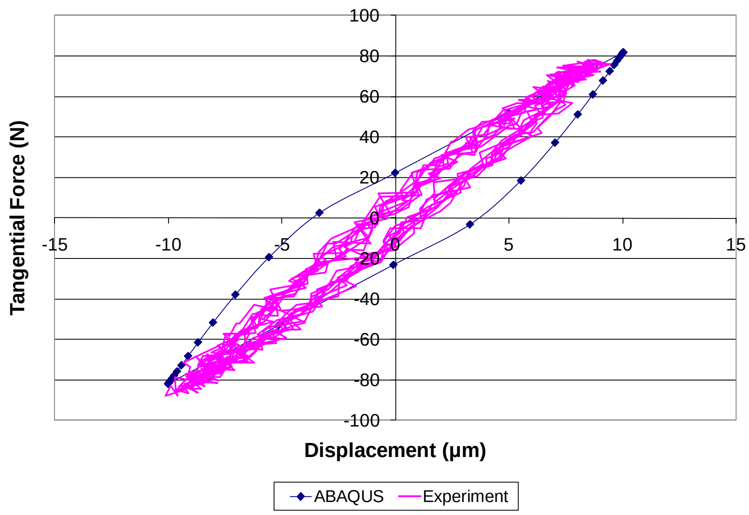

Figure 17. Example of hysteresis response with poorly tuned model properties.

5. Results

The agreement between model and experimental hysteresis loops after tuning the stiffness and PTFE-stationary specimen COF is shown in Figure 18. Experimental hysteresis loops were plotted for three consecutive cycles to show the typical variation. The optimal value of the COF against the PTFE layer was found to be 0.04, which is a physically realistic value for contact between steel and PTFE. The optimal stiffness of the compliant layers was determined to be 375 MPa.

These values were determined by comparison with results using 52100 steel as the moving specimen, and were found to be appropriate for use with an A356 aluminum moving specimen as well, shown in Figure 18 (b). Intuitively this should be the case, since the machine compliance should be independent of the choice of the moving specimen material.

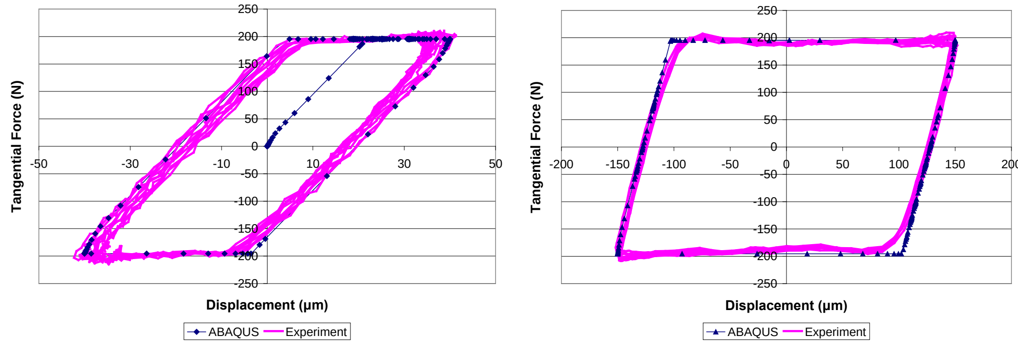

(a) (b)

Figure 18. Comparison of model and experimental hysteresis loops for contact with (a) 52100 steel and (b) A356 aluminum.

The model is able to accurately represent both partial slip and gross slip conditions. The model also demonstrates the transition from partial slip to gross slip conditions at the correct displacement amplitude. The agreement between the hysteresis loops for partial slip and gross slip conditions are shown in Figure 19 where the only difference in the contact parameters is a 10 µm increase in displacement amplitude and a decrease in the COF at the contact between the moving and stationary specimens from 1.22 to 0.78, which are equal to the experimentally measured values. The ability of the model to demonstrate this behavior is a critical aspect in the analysis of the fretting behavior and shows that the model is a good representation of the mechanics of the interaction.

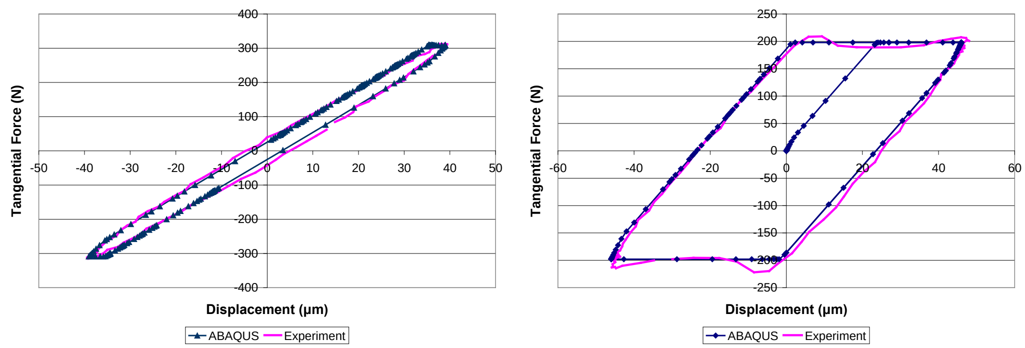

(a) (b)

Figure 19. Model results for modeling of (a) partial slip conditions and (b) gross slip conditions.

A comparison of the predicted hysteresis response using either a Lagrange Multiplier or Penalty friction formulation is shown in Figure 20. The results agree for most regions except at the top left and bottom right corners of the loop. This corresponds to the portion of the cycle where the contact interaction is transitioning from an interfacial condition containing regions of stick and slip to gross sliding. The Lagrange Multiplier friction formulation provides a more accurate solution for this portion of the cycle. Using automatic incrementation resulted in more increments being calculated in those regions for Lagrange Multiplier formulation. The Lagrange Multiplier formulation required 15% more computation time. The computation time for the simulation with a Lagrange Multiplier formulation ranged from 0.5 hours when using a 10 µm displacement amplitude to 1.5 hours for a 100 µm displacement amplitude using a single 3.2 GHz Pentium 4 processor.

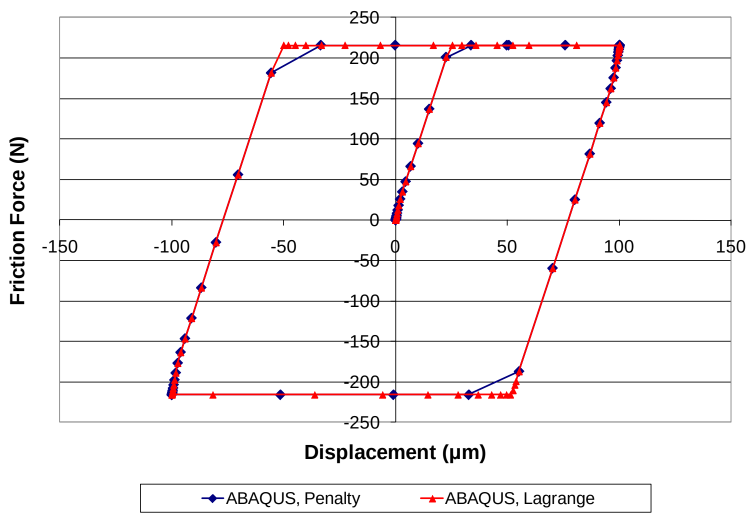

Figure 20. Comparison of the hysteresis loops generated using either the Penalty or Lagrange Multiplier tangential friction formulation.

The Von Mises stress field resulting from the moving specimen sliding to the right is shown in Figure 21 (a). The maximum value occurs at the bottom of the stationary specimen at the interface with the PTFE layer, which was not the expected result. Inspection of the horizontal normal stress as shown in Figure 21 (b) shows that there is a compressive stress at the top surface of the stationary specimen and a tensile stress at the bottom surface. This shows that the specimen is subjected to bending. The PTFE layer that supports the thin stationary specimen easily deforms beneath the contact location, allowing the specimen to bend. The additional tensile horizontal stress at the bottom of the specimen due to bending causes an increase in the Von Mises stress at that location.

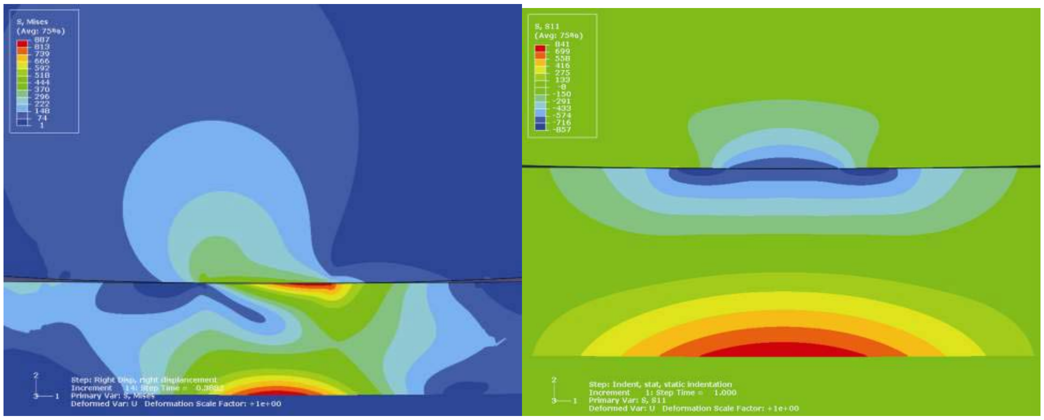

(a) (b)

Figure 21. (a) Von Mises stress while the moving specimen is sliding to the right and (b) horizontal normal stress during indentation.

6. Utilization in design

The cyclically varying multiaxial stress field which results from fretting causes fatigue damage. There have been many studies regarding the extent of damage caused by multiaxial fatigue. These studies have resulted in the development of damage parameters based on the cyclic stress-strain response that indicate the level of fatigue damage. There are several categories of these multiaxial fatigue indicator parameters: Modifications of the Coffin-Manson equation, application of stress or strain invariants, use of the space averages of stress or strain, critical plane approaches, and energy approaches (You and Lee, 1996). Critical plane based multiaxial fatigue damage parameters, which are based on identification of the plane on which the maximum value of a certain combination of stress and strain occurs, have been used successfully as a metric of the extent and location of fatigue damage due to fretting in many studies (Lykins et al., 2000; Vidner and Leidich, 2007; Navarro et al., 2008). Different parameters cater to different materials and loading conditions depending on the dominant damage drivers.

There are also several parameters that have been developed that are specific to fretting damage. These parameters are often based on the amount of energy dissipated due to friction at the interface (Ruiz et al., 1984).

The model of the experimental configuration provides the cyclic stress strain response needed to calculate the fatigue damage parameters. The magnitude of slip output by CSLIP can also be used in conjunction with the contact forces to determine the fretting-specific damage parameters. The values of these parameters can then be correlated to the extent of fatigue damage that was determined experimentally. The correlation between the experimental results and the fatigue indicator parameter values can be used to establish which of the existing parameters best predicts the damage that occurs for different contact conditions. These parameters can also be modified accordingly to better represent the actual material response.

These parameters can serve as a performance metric in design of MLS gaskets. A full scale model of a candidate gasket design can be created and cycled to determine the cyclic stress strain state, contact forces, and magnitude of slip at each point on the part. Thus, the damage metric can be evaluated at each point. Locations with high values of the damage metric will be identified as areas where fretting damage is severe, and the geometry of the gasket at those critical locations can be adjusted in subsequent design iterations.

7. Conclusions

Friction and possible resulting fretting play a major role in modern sealing application for powertrain, exhaust and aftertreatment systems. Destruction of mating surfaces for such applications can have a negative impact on functional and emission performance of those systems. Therefore, it is required to develop technology that helps to develop and design solutions for those sealing applications.

Experimental techniques were developed in order to generate the necessary material properties for thin sheet metal used in MLS gasket applications. These properties are the basis for a simulation-based approach to predict the friction behavior in powertrain and exhaust sealing applications.

This work shows a simple approach that has been developed to analyze the fretting behavior of gaskets. This approach will be implemented into the specific powertrain and exhaust system applications as a standard approach.

8. References

1. Blanchard, P., C. Colombie, V. Pellerin, S. Fayeulle and L. Vincent, "Material Effects in Fretting Wear: Application to Iron, Titanium and Aluminum Alloys," Metallurgical Transactions A (Physical Metallurgy and Materials Science), vol. 22A, pp. 1535-1544, 1991.
2. Deshpande, A., F. Popielas, C. Prior, R. Ramkumar and K. Shaver, "Thermal and System Management Approach for Exhaust Systems," Simulia Customer Conference, London, UK, 2009.
3. Fouvry, S., V. Fridrici, C. Langlade, P. Kapsa and L. Vincent, "Palliatives in Fretting: A Dynamical Approach," Tribology International, vol. 39, pp. 1005-1015, 2006.
4. Grafl, D., M. Lemm and F. Popielas, Patent "De 197 13 053", 1997.
5. Hirsch, M. R. and R. W. Neu, "Fretting Behaviour of AISI 301 Stainless Steel Sheet in Full Hard Condition in Contact with AISI 52100 Steel," Tribology - Materials, Surfaces and Interfaces, vol. 2, pp. 3-9, 2008.

6. Hutson, A. L., T. Nicholas, S. E. Olson and N. E. Ashbaugh, "Effect of Sample Thickness on Local Contact Behavior in a Flat-on-Flat Fretting Fatigue Apparatus," International Journal of Fatigue, vol. 23, pp. 445-453, 2001.
7. Johnson, K. L. Contact Mechanics. Cambridge University Press, Cambridge, New York, 1985.
8. Lykins, C. D., S. Mall and V. Jain, "Evaluation of Parameters for Predicting Fretting Fatigue Crack Initiation," International Journal of Fatigue, vol. 22, pp. 703-716, 2000.
9. Navarro, C., S. Munoz and J. Dominguez, "On the Use of Multiaxial Fatigue Criteria for Fretting Fatigue Life Assessment," International Journal of Fatigue, vol. 30, pp. 32-44, 2008.
10. Ruiz, C., P. Boddington and K. Chen, "An Investigation of Fatigue and Fretting in a Dovetail Joint," Experimental Mechanics, vol. 24, pp. 208-217, 1984.
11. Vidner, J. and E. Leidich, "Enhanced Ruiz Criterion for the Evaluation of Crack Initiation in Contact Subjected to Fretting Fatigue," International Journal of Fatigue, vol. 29, pp. 2040-2049, 2007.
12. Waterhouse, R. B., "Fretting Fatigue," International Materials Reviews, vol. 37, pp. 77-97, 1992.
13. You, B.-R. and S.-B. Lee, "A Critical Review on Multiaxial Fatigue Assessments of Metals," International Journal of Fatigue, vol. 18, pp. 235-244, 1996.